Inorganic Chemistry

Article

pubs.acs.org/IC

NiO@ZnO Heterostructured Nanotubes: Coelectrospinning Fabrication, Characterization, and Highly Enhanced Gas Sensing Properties

Lin Xu, Ruifang Zheng, Shuhai Liu, Jian Song, Jiansheng Chen, Biao Dong, and Hongwei Song*

State Key Laboratory on Integrated Optoelectronics, College of Electronic Science and Engineering, Jilin University, Changchun, 130012, People's Republic of China

Supporting Information

ABSTRACT: Novel NiO@ZnO heterostructured nanotubes (NTs) were fabricated by the coelectrospinning method, consisting of external hexagonal ZnO shell and internal cubic NiO NTs. They are carefully investigated by scanning electron microscopy, transmission electron microscopy, scanning transmission electron microscopy, energy-dispersive X-ray spectroscopy mapping, X-ray diffraction, and X-ray photoelectron spectroscopy techniques. A reasonable formation mechanism of the hierarchical NiO@ZnO NTs is proposed, which is discussed from the view of degradation temperature of different polymers and the amount of inorganic salts. They were then explored for fabrication of H_2S gas sensors. The gas sensing test reveals that compared with the pure ZnO, NiO, and the ZnO−NiO mixed gas sensors, hierarchical gas sensor exhibits highly improved sensing performances to dilute hydrogen sulfide (H_2S) gas. The response of the optimum NiO@ZnO NTs sensor to 50 ppm H_2S increases as high as 2.7−23.7 times compared to the other sensors, whereas the response and recovery times also become shorter considerably. These enhanced gas sensing properties are closely related to the change of nanostructure and activity of ZnO and NiO nanocrystals as well as combination of homo- and heterointerfaces in the optimum gas sensor, which are confirmed by a series of well-designed experiments.

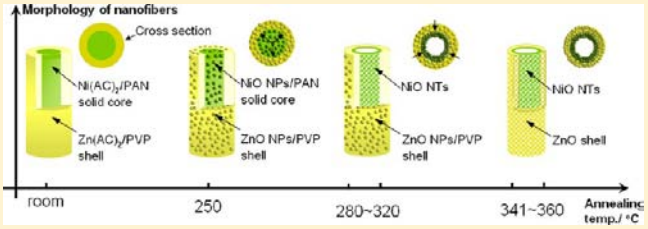

During the past decades, one-dimensional (1D) semiconductor oxides nanomaterials, such as nanowires, nanorods and naotubes (NTs) have captured extensive attention in view of enhancing performance in electrical nanodevices, such as gas sensor, biosensor, solar cell, etc.[1] As a special branches of 1D structure, heterostructured nanomaterials have strong heterointeractions between the closely packed interface nanounits, thus their properties cannot be considered as a simple contacted of the individual components, but more complex and more superior.[2] Recently, Si et al. prepared Fe_2O_3/ZnO heterostructured nanorods by a hydrolysis method, by which considerably enhanced ethanol gas sensing properties were obtained.[2c] Kim et al. prepared SnO_2−In_2O_3 heterostructured nanowires via a thermal evaporation method, and the electronic conductivity of the individual SnO_2−In_2O_3 nanowires was improved by 2 orders of magnitude compared to that of pure SnO_2 nanowires.[2d]

Among various 1D synthesis techniques, coelectrospinning is a simple and scalable method for generating ultralong 1D heterostructure in an efficient, versatile, one-step synthesis. Polymer, organic, inorganic, and hybrid heterostructured materials have been fabricated by this facile method.[3] However, to the best of our knowledge, the heterostructured semiconductor oxide NTs have not been fabricated until now. Actually, heterostructured NTs are very favorable for electrical devices, because it should not only have excellent electrical property like the other 1D nanomaterials but also have a large surface to volume ratio for both the inner and outer layers, as well as the large interface between the two layers. These characteristics make it have potential application in various electrical applications.

Herein, we present the first preparation of the heterostructured semiconductor oxide NTs consisting of inner NiO NTs and outer ZnO shell through coelectrospinning method and its enhanced gas sensing characteristics to H_2S. As is well-known, ZnO is a n-type semiconductor oxide with a wide bandgap (3.37 eV) and large exciton binding energy (60 meV),[4] while NiO is a p-type one with a bandgap of 4.2 eV,[5] and they have been both recognized as excellent gas sensing materials.[6] Moreover, ZnO and NiO can easily form p−n heterojunction and generate an electrical barrier between crystal grains,[7] which can show good sensitivity to reducing gases.[8]

EXPERIMENTAL SECTION

Sample Preparation. The NiO@ZnO heterostructured NTs were fabricated by coelectrospinning followed by calcination, which consisted of following three steps: (a) Preparation of the spinnable precursor outer and inner sol solutions. In a typical procedure, 0.4 g (named as sample ZN1) or 1 g (named as sample ZN2) of zinc acetate with two crystal water ($Zn(Ac)_2$) were dissolved in a mixed solvent composed of 8 mL N,N-dimethylformamide (DMF) and 2 mL

Received: April 12, 2012
Published: June 29, 2012

   dx.doi.org/10.1021/ic300749a | Inorg. Chem. 2012, 51, 7733−7740

ethanol at room temperature. After 15 min, 2 g of poly(vinyl pyrrolidone) (PVP, M_w = 130 000) was added and followed by vigorous stirring for 3 h to obtain the transparent outer sol solutions. In a familiar way, 0.8 g of nickel acetate with four crystal water ($Ni(Ac)_2$) was dissolved in 10 mL of DMF with magnetic stirring for 15 min at room temperature. Subsequently, 1.5 g of poly(acrylonitrile) (PAN, M_w = 150 000) was added into the above solution, followed by vigorous stirring for 12 h to obtain the colorless inner precursor solution. (b) Coelectrospinning the obtained solutions. The schematic diagram of the coelectrospinning setup is illustrated in Figure 1. It consists of three major components: a high-voltage power supply, a syringe pump, and a coaxial spinneret setup. The actual coaxial spinneret is shown in the top inset of Figure 1. The stainless syringe needles marked as # 1 (1.4 mm in diameter) and # 2 (0.7 in diameter) constitute the key part of the coaxial spinneret which connected with outer and inner solutions respectively. The stainless syringe needles marked as # 3 used to transport the outer solution into the outer plastic syringe. The two different solutions were delivered independently through the concentric nozzles with the flow rates controlled by two separate syringe pumps. The feeding rates of outer and inner solution are 0.6 and 0.2 mL/h, respectively. In coelectrospinning process, the collection distance between coaxial spinneret tip and collector is 15 cm and the applied steady-voltage is 15 kV. The obtained coelectrospinning nanowires (see the inset of Figure 1) were collected and dried 12 h at room temperature under vacuum. (c) The thermal treatment. In this process, the coelectrospinning fibers were annealed in a tube furnace with a rising rate of 1 °C/min from room temperature to 700 °C and kept for 3 h, then was self-cooled down to room temperature again, forming the final heterostructured NTs. In addition, to understand the formation mechanism of the as-fabricated NTs nanostructure, we also fabricated some other samples with different amount of $Zn(Ac)_2$ or $Ni(Ac)_2$ and the pure ZnO and NiO for contrast and the preparation details are listed in Supporting Information.

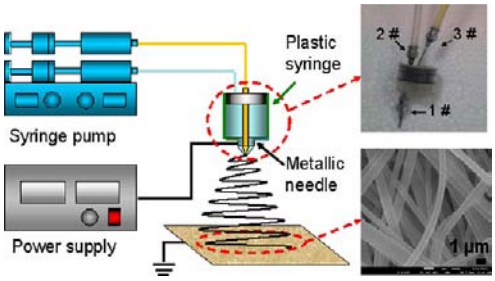

Figure 1. Schematic diagram of the experimental coelectrospinning setup. The insets are the actual photo of the coaxial dual spinnerets (the top one) and the SEM image of the precursor nanofibers (the below one).

Characterization and Measurement. The surface morphology of the as-prepared samples was inspected using a JEOL JSM-7500F scanning electron microscopy (SEM) at an accelerating voltage of 15 kV with gold sputtered on samples. The average diameter of samples was calculated by selecting at least 100 fibers randomly from the SEM micrographs. Transmission electron microscopy (TEM) and scanning transmission electron microscopy (STEM) images were recorded on a JEM-2010 transmission electron microscope under a working voltage of 200 kV equipped with energy dispersive X-ray (EDX) spectrometer. X-ray diffraction (XRD) patterns of the samples were conducted on a Rigaku D/max 2550 X-ray diffractometer, using a monochromatized Cu target radiation resource (λ = 1.5045 Å). X-ray photoelectron spectroscopy (XPS) experiments were measured using an ESCAlab 250 Analytical XPL Spectrometer with a monochromatic Al Kα source. All the binding energies were referenced to the C1s peak at 284.7 eV of the surface adventitious carbon. The fitted peaks in the XPS spectra were deconvoluted using the XPS Peak 4.1 software.

The gas sensing properties were measured on a WS-30A system (Weisheng Instruments Co. Zhengzhou, China). The gas sensors were fabricated by coating the as-prepared NiO@ZnO NTs ethanol colloids on the ceramic tube (the coating thickness is about 0.25 mm) on which a pair of gold electrodes were previously printed. A small spring-like Ni−Cr alloy was inserted into the ceramic tube to provide the operating temperature. The gas sensors were dried and aged for 10 days before the first measurement. When testing, a given amount of target gases together with dry synthetic air were injected into the chamber (about 2.5 L in volume) to obtain desired concentrations. The response is defined as R_{air}/R_{gas} for n-type gas sensors and R_{gas}/R_{air} for p-type gas sensors, where R_{air} and R_{gas} are the resistance for sensors in air and in target gas. The response and recovery times are defined as the time required reaching 90% of the final equilibrium value.

RESULTS AND DISCUSSION

Morphologies and Structural Properties of Hierarchical NiO@ZnO NTs. The NiO@ZnO heterostructured NTs (samples ZN1 and ZN2) as well as the pure ZnO and NiO

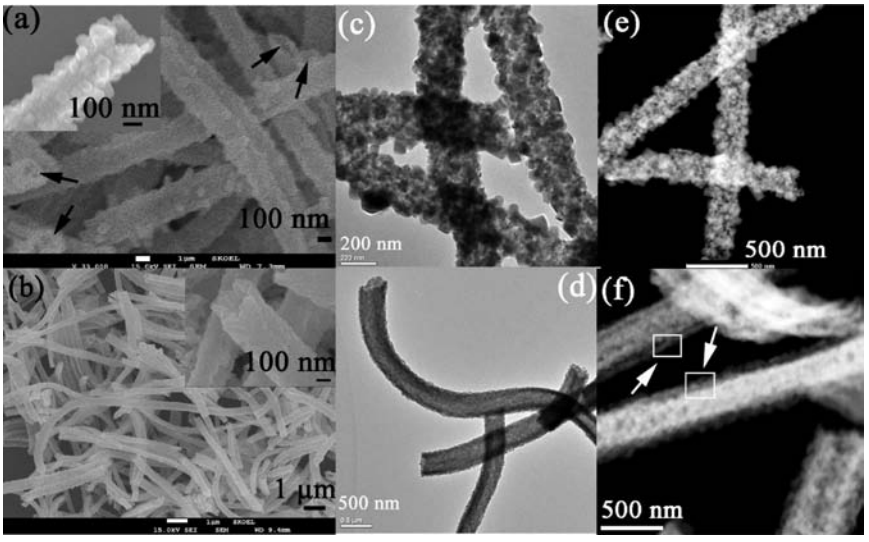

Figure 2. (a, b) SEM, (c, d) TEM, and (e, f) STEM images of core−shell ZN1 and ZN2 NTs, respectively. The insets of panels a and b show the corresponding close-ups of the NTs sections.

dx.doi.org/10.1021/ic300749a | Inorg. Chem. 2012, 51, 7733−7740

nanofibers were fabricated though coelectrospinning method followed by calcination. The SEM images of hierarchical samples ZN1 and ZN2 are shown in Figure 2a,b, respectively. It can be observed that these randomly oriented NTs all have uniform and long continuous surface. In detail, for sample ZN1, the inset of Figure 2a clearly displays the cross section of the obtained NTs with a rough surface, the wall thicknesses are determined to be ∼55 nm and outer diameters are ∼210 nm. Moreover, there are some nanoparticles attached randomly on the surface of the NTs. The morphology of sample ZN2 seems somewhat different. It can be seen that sample ZN2 yields smoother surface with outer diameters ∼310 nm. The NTs structure can also be affirmed by the cross-section SEM images from inset of Figure 2b and the wall thicknesses are determined to be ∼100 nm. TEM and STEM images of sample ZN1 and ZN2 can give more information about the structure characteristics. As shown in Figure 2c,e, the sample ZN1 displays heteroarchitectures and there are some irregular shape implanted on the wall of NTs. In addition, the wall surface where not covered by nanoparticles show a porous structure agglomerated with very small nanocrystals. Note that the porous substructure are formed because of the calcination aimed at removing the polymer, besides, the high annealing temperature is helpful of creating spacings among the nanograins.[9] For sample ZN2 which contains more zinc salt in the outer electrospinning solution, the TEM image (Figure 2d) can further prove its tubular structure. What's important, from STEM image (Figure 2f) the hierarchy structure can be distinguished, which is caused by the differences of reflection and transmission ability of different materials of outer shell and inner NTs.

To further investigate the heteroarchitectures, we conducted the EDX mappings to determine the specific distribution of Ni and Zn elements in hierarchical samples ZN1 and ZN2. As shown in Figure 3, it can be clearly seen that the distribution of Ni elements exhibit a hollow structure and the outer diameters are both ∼210 nm corresponding to samples ZN1 and ZN2, furthermore, the distribution of Ni elements in two samples are homogeneous. While, the distribution of Zn elements exhibit larger diameter than Ni elements. For sample ZN1, the Zn elements are uniform and discontinuous. This demonstrates that Zn elements mainly dispersed on the outer wall of Ni NTs and aggregated to form nanoparticles. Differently, the distribution of Zn elements in sample ZN2 seems homogeneous and continuous, and shows the hollow tubular structure. That is to say, sample ZN2 yields more completed NiO@ZnO heterostructure with both uniform and continued inner NiO NTs and outer ZnO shell. Moreover, the distribution of ZnO can be adjusted by changing the zinc salts content in precursor outer solution as shown in below.

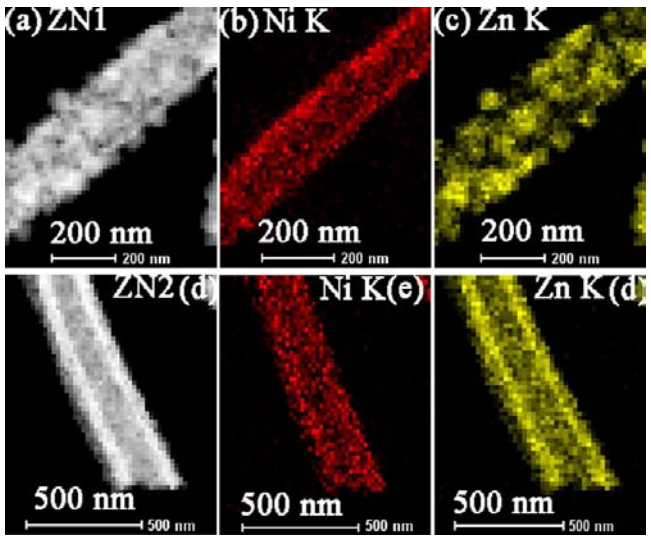

Figure 3. The EDX elemental mapping images of Ni and Zn of sample (a–c) ZN1 and (d–f) ZN2.

The XRD patterns of hierarchical ZN1 and ZN2 NTs compared with pure ZnO and NiO are shown in Figure 4,

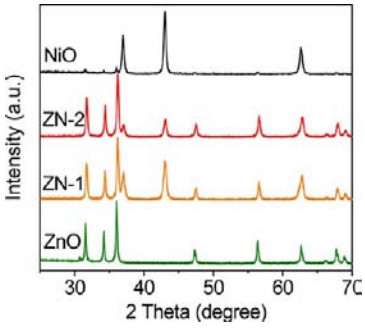

Figure 4. XRD patterns of hierarchical samples ZN1, ZN2, pure ZnO, and NiO.

which provide further insight into the crystallinity of the products. It can be seen that all the samples are well crystallized. Compared with pure ZnO and NiO, the XRD pattern taken from the samples ZN1 and ZN2 can be both indexed to the mixed of cubic NiO (JCPDS card: 78−0643) and hexagonal ZnO (JCPDS card: 36−1451) with separate phases and no obvious peak shift or any trace of other phases can be detected. Besides, because of the different initial $Zn(Ac)_2$ content in samples ZN1 and ZN2, the main XRD peaks of cubic NiO and hexagonal ZnO in each nanocomposite are different. Moreover, the relative intensity of the dominant diffraction peak of ZnO is always higher than that of NiO, even in the sample whose molecular weights of ZnO and NiO are almost the same (sample ZN2), indicating the good crystallinity of ZnO in hierarchical sample ZN2.

XPS Spectra: Surface States and Interface Interaction. To further illuminate the surface composition and chemical state of the elements existing in hierarchical NiO@ZnO NTs samples, we studied XPS spectra of samples ZN1 and ZN2 as well as pure ZnO and NiO. As shown in Figure 5a, the complete spectra of samples ZN1 and ZN2 confirm the presence of Zn, Ni, O, and C atoms. The peak at 284.7 eV is attributed to the adventitious carbon based contaminant adsorbed on the surfaces of the NTs.[10] As is shown, when the content of different components changes in the studied ZN1 and ZN2 samples, the intensities of the ZnO and NiO characteristic peaks also change in the same trend.

The O 1s XPS spectra of various samples are enlarged in Figure 5b. Accordingly, The XPS spectra of O1s core level electrons measured from pure ZnO and NiO both display there peaks. The binding energies of 529.4 in NiO and 530.2 in ZnO correspond to the lattice oxygen in crystalline NiO and ZnO, respectively. The O 1s peak at 531.9 eV is assigned to the deficient oxygen and the peak at 532.7 eV belongs to the chemisorbed or dissociated oxygen or OH species on the

dx.doi.org/10.1021/ic300749a | Inorg. Chem. 2012, 51, 7733−7740

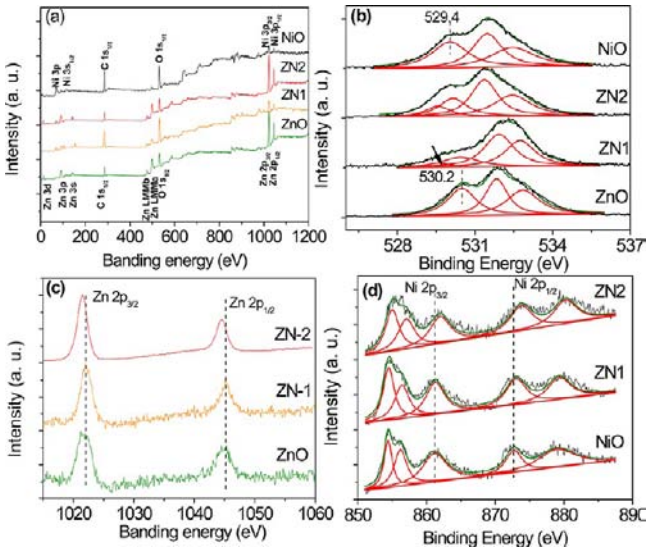

Figure 5. (a) Survey, (b) O 1s, (c) Zn 2p, and (d) Ni 2p high-resolution XPS spectra of samples ZN1, ZN2, pure ZnO, and NiO.

samples surface.[11] The samples ZN1 and ZN2 can both be well dissolved by four components, locating at ~529.6, 530.4, 531.9, and 532.7 eV, respectively. Note that because the different chemical environment of O in composite oxides, each characteristic peak has some shift in the two samples. Moreover, defective oxygen occupies the biggest proportion in both samples, suggesting a large number of surface oxygen vacancies. The atomic ratio percentages of deficient oxygen of O 1s are calculated as 30.4%, 33.8%, 39.1, and 43.7% for NiO, ZnO, ZN1, and ZN2 respectively. Generally, when the ZnO and NiO nanocrystals attach continuously, their corresponding Fermi energy levels would be adjusted to the same value. The electrons transferred from ZnO to NiO, while the hole transferred from NiO to ZnO due to the carrier diffusion caused by the concentration gradient near the p-n junction. This diffusion process leads to the higher valence concentration of ZnO. Besides, it is obvious that the relative intensity of lattice oxygen of NiO in sample ZN2 is much lower than that in sample ZN1 though they have the same amount of NiO. This can be explained by NiO being coated by external ZnO more effectively in sample ZN2.

The characteristic spin−orbit split X-ray photoelectron spectroscopy (XPS) data of Zn 2p core level region of hierarchical ZN1, ZN2 and pure ZnO samples are given in Figure 5c. The Zn 2p spectrum in all the samples show two symmetric peaks, the peak centered at 1022.1 eV corresponds to the Zn $2p_{3/2}$ and another one centered at 1045.1 eV is assigned to Zn $2p_{1/2}$, indicating a normal state of Zn 2p in the pure ZnO NTs.[12] Compared to pure ZnO, the Zn 2p core level region of hierarchical sample ZN1 has no significant shift. For sample ZN2, the Zn 2p peaks shift to the low binding energy obviously after introducing of NiO, but with the same splitting between Zn $2p_{1/2}$ and Zn $2p_{3/2}$ (23 eV). Ni 2p electron core level XPS spectra of hierarchical ZN1, ZN2 and pure NiO samples are shown in Figure 5d. For the pure NiO, the Ni 2p signal could be deconvoluted into five peaks.[13] The peaks at 854.5, 856.2, and 861.2 eV were attributed to Ni $2p_{3/2}$, and the peaks at 872.7 and 879.1 eV to Ni $2p_{1/2}$. The Ni 2p peaks of sample ZN1 and ZN2 can also be deconvoluted into five ones, and the spectrum of sample ZN2 also exhibits overall shift to higher binding energy in contrast to pure NiO as well as sample ZN1. The shift of Zn 2p peaks to lower binding energy is about 0.9 eV and Ni 2p peaks to higher binding energy is about 0.7 eV compared with the corresponding value for pure ZnO or NiO samples respectively, which are comparable or even larger than the binding energy shifts in nanocomposite ZnO−NiO nanofibers (0.9 eV for Zn 2p and 0.5 eV for Ni 2p).[14] This phenomenon can be explained by the strong interaction between ZnO and NiO nanocrystals in sample ZN2,[15] It will lead to the increased surface activity of ZnO nanocrystals and the decreased surface activity of NiO nanocrystals.

Formation Mechanism of Hierarchical NiO@ZnO NTs. Herein, we discuss the formation mechanism of the as-fabricated hierarchical NiO@ZnO NTs from the view of reaction temperature and the ratio of inorganic salts to polymers. Our previous studies about electrospinning NTs structure indicate that the ratio of inorganic salts to polymer and slowly annealing temperature are key factors for the formation of NTs.[16] In this case, due to the incompatibility of PVP and PAN, the initial hierarchical solid core−shell structure has already been formed in precursor nanofibers.[3] When at a slow rising rate (1 °C/min) in the annealing process, the electrospun solid gel fibers could be homogeneously heated from the surface to the center.[17] According to the literatures, the degradation temperatures of $Zn(Ac)_2$ in PVP and $Ni(AC)_2$ in PAN are both ~250 °C,[18] the degradation temperature range of PAN is 280−320 °C,[19] and that of PVP is 343−361 °C.[17,18a] This means that small ZnO and NiO nanoparticles would be formed (~250 °C) before the removing of PAN and PVP, and the PAN core would decompose (280−320 °C) earlier than the PVP shell (343−361 °C). Moreover, it was previously observed that in the mixture of PVP and PAN nanofibers, the degradation temperature of PVP (389 °C) and PAN (360 °C) both increase than pure PVP and PAN nanofibers because of the reduced interactions between ions and polymers.[19b,20] In the present coelectrospinning, we have reason to consider that the degradation temperature of PVP and PAN on or near the interface of outer and inner layers would be higher than the internal, because the boundary of PVP and PAN is not so distinct.

On the basis of the above analysis, the formation process of hierarchical NiO@ZnO NTs is proposed, as shown in Figure 6.

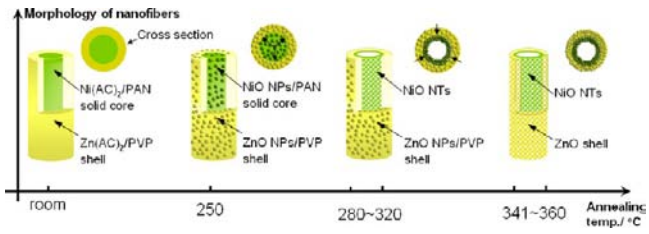

Figure 6. Illustrative diagram of the possible formation process of heterostructured NTs through slow heat treatment procedure.

When the temperature gradually increased from room temperature to 250 °C, $Zn(Ac)_2$ and $Ni(Ac)_2$ first begun to decompose to small ZnO and NiO nanocrystals in outer PVP and inner PAN templates, respectively (see Figure 6). As the annealing temperature was gradually elevated to 280−320 °C, the core PAN started to break down from inner to the interface, while the external PVP shell still existed. At this time, the PVP shell and the interface PAN played a role as template for distribution of internal NiO nanoparticles and made these NiO nanoparticles gathered along the inner wall of the shell. When

dx.doi.org/10.1021/ic300749a | Inorg. Chem. 2012, 51, 7733−7740

the amount of NiO was appropriate, the internal NiO nanoparticles formed tubular structure and gathered closely to the external shell. Note that this process can be proved by Figure 3 together with Figure 7a, when only electrospun the

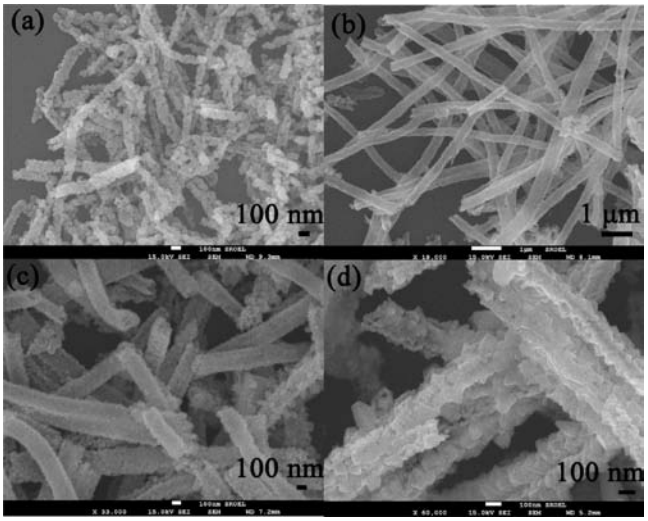

Figure 7. SEM images of (a) pure NiO, (b) pure ZnO, (c) sample ZN3, and (d) sample ZN4.

inner solution (contained 0.8 g $Ni(Ac)_2$), tubular structure NiO could not be formed (see Figure 7a), while it was formed in coelectrospinning case (see Figure 3) and when only electrospun the outer solution (contained 1.0 g $Zn(Ac)_2$), the NTs structure was formed (see Figure 7b). These phenomena indicate the template effect of external shell to internal NTs. When the annealing temperature was further increased to 343−361 °C, the outer PVP started to degrade and form the final product. Because the PVP on the interface had higher degradation temperature, the ZnO nanoparticles distributed alone the internal NTs. As the amount of ZnO nanoparticles were lower, the ZnO were too little to cover the inner NiO NTs completely (sample ZN1). While the amount of ZnO nanoparticles were suitable, the ZnO covered on the inner NiO NTs uniformly and continuously (sample ZN2). When the amount of ZnO nanoparticles were not suitable enough, a mixture nanostructure of ZN1 and ZN2 was formed, as shown in Figure 7c. This further demonstrates that when the amount of NiO was appropriate, the external amount of ZnO nanoparticles could not affect the inner NTs structure and they just distributed on the inner NTs wall in different forms. That is, the internal NiO NTs had been already formed before the distribution of ZnO nanoparticles. In addition, when the amount of internal NiO decreased, no continuous NTs were formed during the decomposition of PAN (Figure 7d), the final morphology did not show the hierarchical structure, which further proved the template effect of internal NiO NTs to the outer shell.

Gas Sensing Properties of Hierarchical NiO@ZnO NTs. In this work, the as-synthesized hierarchical NiO@ZnO NTs samples were fabricated to gas sensors and the gas sensing properties toward to H_2S are carefully investigated. Here, in order to better understanding the gas sensing properties of hierarchical NiO@ZnO NTs, we also fabricated the composite NTs composed of the same ZnO and NiO content as sample ZN2, but ZnO and NiO are mixed uniformly (sample ZN-mix), the corresponding prepared condition and the SEM image are shown in Supporting Information.

First, the responses of the hierarchical NiO@ZnO NTs and different reference gas sensors to 50 ppm H_2S as a function of the working temperature were studied, as shown in Figure 8.

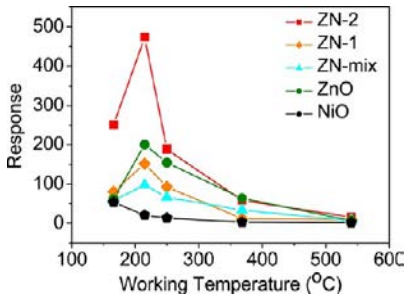

Figure 8. Response of heterostructured ZN1 and ZN2 NTs gas sensors, the mixed ZN-mix NTs gas sensor and pure ZnO and NiO gas sensors to 50 ppm H_2S as a function of operating temperature.

Because of the different amount and contact form of n-type ZnO and p-type NiO in hierarchical samples ZN1, ZN2, and nanocomposite sample ZN-mix, ZN1 and ZN-mix gas sensors show a typical gas sensing characteristics of p-type semiconductor and the response is calculated by R_{gas}/R_{air}, while ZN2 gas sensor shows a typical n-type gas sensing characteristics of semiconductor and the response is calculated by R_{air}/R_{gas}. As can be seen, excepted NiO, the responses for the other gas sensors all have the same change trend. The responses first increase with temperature and approach at the maxima at 215 °C, then gradually decrease with further increasing the working temperature. The response of different gas sensors at 215 °C are response(ZN2) = 474 > response(ZnO) = 200 > response(ZN1) = 152 > response(ZN-mix) = 98 > response(NiO) = 20.8. The response of ZN2 gas sensor is 2.7−23.7 times higher than the other gas sensors.

To further confirm the versatility of the as-synthesized gas sensors, the selective test toward to 50 ppm H2S, H2, NH3 and 200 ppm acetone and methanol were conducted at 215 °C. As demonstrated in Figure 9, the sensors show excellent selectivity

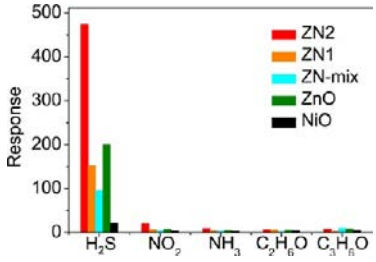

Figure 9. Selective test toward 50 ppm H_2S, NO_2, and NH_3, 200 ppm ethanol, and acetone gases of different gas sensors at 215 °C.

to H_2S, whereas they have almost no response to the other typical interference gases at the same temperature. This indicates that the present sensors have quite excellent selectivity to the H_2S, especially the ZN2 one. The prominent selectivity can be assigned to theirs particular gas sensing mechanism, which will be discussed below.

Figure10a shows response transients of different gas sensors exposed to 50 ppm H_2S gas. The ZN2 sensor exhibits the fastest switching dynamics to H_2S at the optimal temperature.

dx.doi.org/10.1021/ic300749a | Inorg. Chem. 2012, 51, 7733−7740

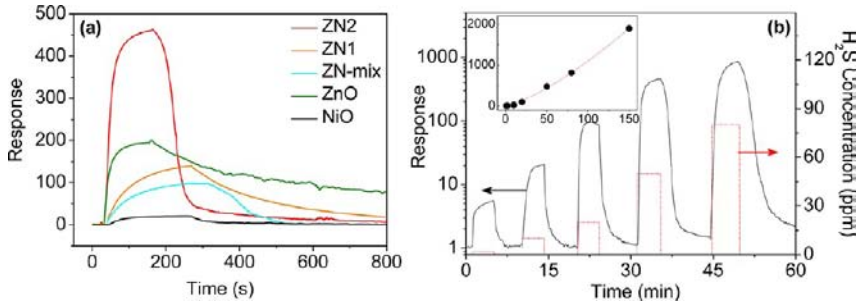

Figure 10. (a) Response transients of different gas sensors to 20 ppm H_2S at 215 °C. (b) Dynamic process of ZN2 gas sensor to different H_2S concentrations (2−80 ppm) at 215 °C, the inset shows the corresponding sensor response curves (1−150 ppm) and the red line is the fit one.

Its response time is ∼50 s and recovery time is ∼124 s. For the ZnO gas sensor, although the response time is comparable to ZN2, the recovery time of the sensor is too long (∼1254s) and cannot return to its original state in time. And the other gas sensors (ZN1, ZN-mix, and NiO gas sensors) show more slower dynamic processes, the response and recovery times are ∼82 and 191 s for ZN1, ∼132 and 204 s for ZN-mix, and ∼112 and 200 s for NiO gas sensors. Figure 10b shows the dynamic response of ZN2 hierarchical NTs gas sensor exposed to different concentrations of H_2S around 215 °C, which indicates it exhibits rapid switching dynamics to H_2S at the optimal temperature and the excellent reproducible performance. The inset of Figure 10b shows the corresponding relationship between the sensor responses and gas concentrations (1−150 ppm) of H_2S gases. The response to 150 ppm H_2S is as high as 1891. The response and target gas concentration (C_{gas}) can be approximated fitted by an empirically equation, response = $1 + \alpha C_{gas}^{\beta}$ with $\beta = 1.36 \pm 0.10$.[21] Here, β was determined to be (1.36 ± 0.10) for ZN2 gas sensors, which was much higher than empirical value (0.5 or 1).[21] Moreover, the on- and off-responses could be repeated after continuous measurement cycles without observing significant variation in the functional response, illustrating the good reversibility and stability of the hierarchical structure-based gas sensor.

The dependence of response and recovery times to 50 ppm H_2S of ZN2 gas sensor compared with pure ZnO and NiO gas sensors on working temperature was also studied. Figure 11

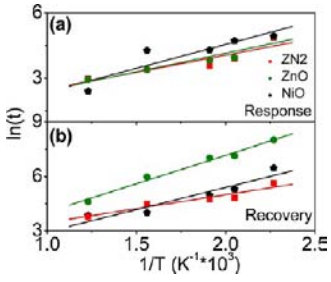

Figure 11. Logarithm of (a) the response time constant and (b) recovery time constants (both in second) at 215 °C to 50 ppm H_2S versus the reverse of temperature. The dots are experimental data and the lines are the corresponding linear fitting functions.

shows in the form of the logarithm of time constants versus the reverse of absolute temperature. Using the well-known thermal activation function, we can be calculate the response (ΔE_{res}) and recovery (ΔE_{rec}) barrier heights through the temperature-dependence of response and recovery dynamics.[22] Accordingly, ΔE_{res} values are determined to be 98, 107, and 138 meV, ΔE_{rec} values to be 133, 270, and 211 meV, respectively, for the ZN2, ZnO, and NiO gas sensors. As is well-known, the lower barrier heights are, the easier of the response and recovery reactions to take place. That is to say, response and recovery reactions are easier to happen in ZN2 gas sensor than in the pure sensors. It should be mentioned that the recovery time can be hardly measured for ZN1 and ZN-mix gas sensor for all the working temperature, indicating a huge ΔE_{rec} values for those two samples.

Table 1 lists the performance of H_2S gas sensor based on various nanostructures that contained ZnO or NiO in the literatures and ZN2 hierarchical NTs in this study. Comparing our results with these literatures, it can be found that ZN2 hierarchical NTs gas sensor exhibits much better response to most of the other sensors except the ZnO nanorods gas sensor reported by ref 23e. It should be also noted that although the response of the sensor listed in ref 23e is super high at 150 °C, it cannot return to its original state unless the operating temperature is increased to 450 °C. The present ZN2 sensor yields not only high response but also favorable fast response and recovery times.

Table 1. Comparison of the H_2S Gas Sensors Contained ZnO or NiO in Literatures to the ZN2 NT Sensor in This Work

samples	gas conc. (ppm)	T (°C)	response	ref
ZnO-TiO_2 nanocrystals	10 000	250	2.5	23a
ZnO-WO_3 film	3.5	260	1.4	23b
Cu doped ZnO nanofibers	10	230	18.7	23c
ZnO nanofibers	10	230	1.57	23c
ZnO nanorods	50	500	29	23d
ZnO nanorods	20	150	4000	23e
ZnO dendrites	100	30	17.3	23f
NiO nanoparticles	100	150	9	23g
ZN2 NTs	50	215	474	This work

Generally, there exist two possible mechanisms for semiconductor oxide-based H_2S gas sensors: adsorption−oxidation−desorption process and the sulfuration−desulfuration process.[23c,e] In this experiment, the relative lower working temperature, shorter dynamic process, higher response to low concentrate H_2S gas, and excellent selectivity are all characteristics of the sulfuration−desulfuration process.[22,23d,e] The possible reason that responsible for the enhanced gas sensing properties of the ZN2 sensor for H_2S can be mainly attributed to the variation of nanostructure and surface activity of ZnO and NiO nanocrystals in different gas sensors. For ZN2 sample,

dx.doi.org/10.1021/ic300749a | Inorg. Chem. 2012, 51, 7733−7740

because of the particular continuous nanostructure of both inner NiO and outer ZnO which has suitable contacted area, appropriate p−n junctions are formed and created strong interaction as proved by XPS data. For sample ZN1, as a result of the discontinuous distribution of ZnO nanocrystals on the NiO NTs, the contact areas of NiO and ZnO are too small to make significant interaction. Although for the sample ZN-mix, which also has obvious interaction,[14] the corresponding sensor shows much weaker gas sensing properties because of the different distributed ways of ZnO and NiO nanocrystals in nanostructure and bring the sensing properties of n-type ZnO and p-type NiO cancel each other out. In other words, from the above analysis, we can get the conclusion that the nanostructure like ZN2, which contained a suitable contact area and distribution way of NiO and ZnO is an optimal one. From the view of surface activity of ZnO and NiO nanocrystals in different gas sensors, the ZN2 sensor shows a typical gas sensing characteristics of n-type semiconductor, that is to say, ZnO are the dominant influence factor to its gas sensing properties. As previously discussed in XPS spectra, the activity of ZnO in the ZN2 gas sensor increases because of the strong interaction between ZnO and NiO nanocrystals, and thus the sulfuration−desulfuration process can take place easier, which results in the improved gas sensing properties to H_2S; this can be further proved by the lower ΔE_{res} and ΔE_{rec} values of ZN2 gas sensor (Figure 11). ZN1 and ZN-mix gas sensors show the p-type gas sensing behavior, that is, NiO is the main effect factor to their gas sensing properties. On the one hand, the tendency of sulfuration reaction of NiO is weaker than ZnO due to the Gibbs free energy (ΔG) value of these two sulfuration reactions ($NiO + H_2S = NiS + H_2O$; $ZnO + H_2S = ZnS + H_2O$) are −61.6 and −75.3 kJ mol^{-1} respectively. On the other hand, the activity of NiO in ZN1 and ZN-mix gas sensors only has little change or even much more stable (as proved by XPS data), thus the gas sensing properties are no better than ZN2 gas sensor and even lower than the pure ZnO gas sensor.

In addition, in nanofiber gas sensors the contact way of nanofiber networking also influence the gas sensing properties. In hierarchical ZN2 samples, combination of homo- (between the NTs) and hetero- (between the ZnO and NiO) interfaces are formed, which may build the potential barriers in the junctions and improved the corresponding gas properties.[24] However, in the other sensors, there are only the homointerfaces (ZnO and NiO gas sensors) or heterointerfaces (ZN-mix gas sensors) formed at the junctions.

CONCLUSIONS

In summary, novel hierarchy structure n-type ZnO and p-type NiO NTs were fabricated using a facile coelectrospinning technique. The hierarchical NiO@ZnO NTs possess a hexagonal ZnO phase in the outer shell and a cubic NiO phase in the inner NTs. Through controlling the ratio of ZnO to NiO, we modulated the morphology of NTs, from the external ZnO uncompleted coverage to entirely covered state on the internal NiO NTs. The formation mechanism of ZnO-NiO NTs was discussed. Moreover, the XPS spectra indicate the strong interaction of ZnO and NiO on the interface. The H_2S gas sensing properties based on the hierarchy NiO@ZnO NTs was studied. The results demonstrate that the different ratio and distributed of ZnO to NiO have great effect on the gas sensing behavior. ZN2 gas sensor is the outstanding one, it shows higher response, excellent selectivity and faster dynamic process, and lower barrier height. The present work suggests that the suitable nanostructure, increased activity of ZnO nanocrystals and combination of homo- and heterointerfaces endowed the NiO@ZnO NT gas sensor with highly enhanced gas sensing properties.

ASSOCIATED CONTENT

Supporting Information

The detailed procedure of each reference sample and SEM images of sample ZN-mix. This material is available free of charge via the Internet at http://pubs.acs.org.

AUTHOR INFORMATION

Corresponding Author

*Phone and fax: +86-431-85155129. E-mail: hwsong2005@yahoo.com.cn.

Notes

The authors declare no competing financial interest.

ACKNOWLEDGMENTS

The authors are thankful for the financial support of the National Science Fund for Distinguished Young Scholars of China (Grant 60925018), the National Natural Science Foundation of China (Grants 51002062, 61177042, and 11174111), the Frontier Science and Interdisciplinary Innovation Projects of Jilin University (Grants 421030951419).

REFERENCES

(1) (a) Law, M.; Greene, L. E.; Johnson, J. C.; Saykally, R.; Yang, P. D. *Nat. Mater.* **2005**, *4*, 455−459. (b) Sun, L. L.; Zhao, D. X.; Zhang, Z. Z.; Li, B. H.; Shen, D. Z. *J. Mater. Chem.* **2011**, *21*, 9674−9681. (c) Chen, J.; Xu, L.; Li, W. Y.; Gou, X. L. *Adv. Mater.* **2005**, *17*, 582−586. (d)

(2) (a) Lauhon, L. J.; Gudiksen, M. S.; Wang, D.; Lieber, C. M. *Nature* **2002**, *420*, 57−61. (b) Hwang, Y. J.; Boukai, A.; Yang, P. D. *Nano Lett.* **2009**, *9*, 410−415. (c) Si, S. F.; Li, C. H.; Wang, X.; Peng, Q.; Li, Y. D. *Sens. Actuators, B* **2006**, *119*, 52−56. (d) Kim, D. W.; Hwang, I. S.; Kwon, S. J.; Kang, H. Y.; Park, K. S.; Choi, Y. J.; Choi, K. J.; Park, J. G. *Nano Lett.* **2007**, *7*, 3041−3045. (e) Hou, Z. Y.; Li, C. X.; Ma, P. G.; Li, G. G.; Cheng, Z. Y.; Peng, C.; Yang, D. M.; Yang, P. P.; Lin, J. *Adv. Funct. Mater.* **2011**, *21*, 2356−2365. (f) Hou, Z. Y.; Li, G. G.; Lian, H. Z.; Lin, J. *J. Mater. Chem.* **2012**, *22*, 5254−5276.

(3) (a) Chen, M. L.; Dong, M. D.; Havelund, R.; Regina, V. R.; Meyer, R. L.; Besenbacher, F.; Kingshott, P. *Chem. Mater.* **2010**, *22*, 4214−4221. (b) Magalhaes, W.; Cao, X. D.; Lucia, L. A. *Langmuir* **2009**, *25*, 13250−13257. (c) Gu, Y. X.; Chen, D. R.; Jiao, X. L.; Liu, F. F. *J. Mater. Chem.* **2007**, *17*, 1769−1776. (d) Kurban, Z.; Lovell, A.; Bennington, S. M.; Jenkins, D. W. K.; Ryan, K. R.; Jones, M. O.; Skipper, N. T.; David, W. I. F. *J. Phys. Chem. C* **2010**, *114*, 21201−21213.

(4) Gu, Z. J.; Paranthaman, M. P.; Xu, J.; Pan, Z. W. *ACS Nano* **2009**, *3*, 273−278.

(5) Moreira, I. R.; Illas, F.; Martin, R. L. *Phys. Rev. B* **2002**, *65*, 155102.

(6) (a) Li, J.; Fan, H. Q.; Jia, X. H. *J. Phys. Chem. C* **2010**, *114*, 14684−14691. (b) Wu, H.; Lin, D. D.; Zhang, R.; Pan, W. *Chem. Mater.* **2007**, *19*, 1895−1897.

(7) Ohta, H.; Hirano, M.; Nakahara, K.; Maruta, H.; Tanabe, T.; Kamiya, M.; Kamiya, T.; Hosono, H. *Appl. Phys. Lett.* **2003**, *5*, 1029−1031.

(8) Wang, Z. J.; Li, Z. Y.; Sun, J. H.; Zhang, H. N.; Wang, W.; Zheng, W.; Wang, C. *J. Phys. Chem. C* **2010**, *114*, 6100−6105.

(9) Chen, W. S.; Huang, D. A.; Chen, H. C.; Shie, T. Y.; Hsieh, C. H.; Liao, J. D.; Kuo, C. S. *Cryst. Growth Des.* **2009**, *9*, 4070−4077.

(10) Zhang, Y. W.; Si, R.; Liao, C. S.; Yan., C. H. *J. Phys. Chem. B* **2003**, *107*, 10159−10167.

(11) Erdem, B.; Hunsicker, R. A.; Simmons, G. W.; Sudol, E. D.; Dimonie, V. L.; El-Aasser, M. S. *Langmuir* **2001**, *17*, 2664−2669.
(12) Ge, L.; Jing, X. Y.; Wang, J.; Wang, J.; Jamil, S.; Liu, Q.; Liu, F.; Zhang, M. *J. Mater. Chem.* **2011**, *21*, 10750−10754.
(13) Ding, Y.; Wang, Y.; Su, L.; Zhang, H.; Lei, Y. *J. Mater. Chem.* **2010**, *20*, 9918−9926.
(14) Zhang, Z. Y.; Shao, C. L.; Li, X. H.; Wang, C. H.; Zhang, M. Y.; Liu, Y. C. *ACS Appl. Mater. Inter.* **2010**, *2*, 2915−2923.
(15) Lin, D. D.; Wu, H.; Zhang, R.; Pan, W. *Chem. Mater.* **2009**, *21*, 3479−3484.
(16) Xu, L.; Song, H. W.; Dong, B.; Wang, Y.; Bai, X.; Wang, G. L.; Liu, Q. *J. Phys. Chem. C* **2009**, *113*, 9609−9615.
(17) Mou, F. Z.; Guan, J. G.; Shi, W. D.; Sun, Z. G.; Wang, S. H. *Langmuir* **2010**, *26*, 15580−15585.
(18) (a) Teh, P. F.; Sharma, Y.; Pramana, S. S.; Srinivasan, M. *J. Mater. Chem.* **2011**, *21*, 14999−15008. (b) Ji, L. W.; Lin, Z.; Alcoutlabi, M.; Toprakci, O.; Yao, Y. F.; Xu, G. J.; Li, S. L.; Zhang, X. W. *RSC Adv.* **2012**, *2*, 192−198.
(19) (a) Kim, C.; Ngoc, B.; Yang, K. S.; Kojima, M.; Kim, Y. A.; Kim, Y. J.; Endo, M.; Yang, S. C. *Adv. Mater.* **2007**, *19*, 2341−2346. (b) Ji, L. W.; Lin, Z.; Li, Y.; Li, S. L.; Liang, Y. Z.; Toprakci, O.; Shi, Q.; Zhang, X. W. *Polymer* **2010**, *51*, 4368−4374.
(20) Zhang, Z. Y.; Li, X. H.; Wang, C. H.; Wei, L. M.; Liu, Y. C.; Shao, C. L. *J. Phys. Chem. C* **2009**, *113*, 19397−19403.
(21) Wang, J. X.; Sun, X.; Huang, W. H.; Lee, Y. C.; Tan, O. K.; Yu, M. B.; Lo, G. Q.; Kwong, D. L. *Appl. Phys. A: Mater. Sci. Process.* **2007**, *88*, 611−615.
(22) Xu, L.; Dong, B.; Wang, Y.; Bai, X.; Liu, Q.; Song, H. W. *Sens. Actuat. B* **2010**, *147*, 531−538.
(23) (a) Bodade, A. B.; Bende, A. M.; Chaudhari, G. N. *Vacuum* **2008**, *82*, 588−593. (b) Stankova, M.; Vilanova, X.; Calderer, J.; Llobet, E.; Brezmes, J.; Gracia, I.; Cane, C.; Correig, X. *Sens. Actuators, B* **2006**, *113*, 241−248. (c) Zhao, M. G.; Wang, X. C.; Ning, L. L.; Jia, J. F.; Li, X. J.; Cao, L. L. *Sens. Actuators, B* **2011**, *156*, 588−592. (d) Kim, J.; Yong, K. *J. Phys. Chem. C* **2011**, *115*, 7218−7224. (e) Wang, D.; Chu, X. F.; Gong, M. L. *Nanotechnology* **2007**, *18*, 185601. (f) Zhang, N.; Yu, K.; Li, Q.; Zhu, Z. Q.; Wan, Q. *J. Appl. Phys.* **2008**, *103*, 104305. (g) Du, Y.; Wang, W.; Li, X. L.; Zhao, J.; Ma, J. M.; Liu, Y. P.; Lu, G. Y. *Mater. Lett.* **2012**, *68*, 168−170.
(24) Choi, S. W.; Park, J. Y.; Kim, S. S. *Nanotechnology* **2009**, *20*, 465603.